Pergamon

Journal of Structural Geology, Vol. 16, No. 8, pp. 1173 to 1186, 1994

0191-8141/94 $07.00+0.00

0191-8141(93)E0009-A

Three-dimensional numerical simulations of crustal-scale wrenching using a non-linear failure criterion

JEAN BRAUN

Research School of Earth Sciences, Australian National University, GPO Box 4, Canberra, ACT 2601, Australia

(*Received* 27 *January* 1993; *accepted in revised form* 28 *October* 1993)

Abstract—We have developed a three-dimensional finite element model to study wrench deformation of the crust regarded as an elasto-plastic material obeying Murrell's extension of Griffith's failure criterion.

Numerical experiments using this model predict that the imposed basal wrenching is accommodated by an array of oblique Riedel-like shears and *Y*-shears (parallel to the direction of wrenching). The partitioning of deformation between the two types of structure depends on the width of the zone of imposed basal wrenching and the existence of a component of deformation in the *x*-direction (normal to the direction of wrenching).

The Riedel shears are arranged in spiral-like structures that root into the basal wrench zone. In cross-section, the Riedel shears resemble wedge-shaped flower structures similar to those often observed in seismic cross-sections. The 'polarity' of the flower structures is positive (or palm-tree-like) in transpression experiments and negative (or tulip-like) in transtension experiments. The orientation of the Riedel shears throughout the crust obeys Mohr's hypothesis for incipient faulting combined with Murrell's failure criterion.

The model also predicts plastic dilatancy inversely proportional to the square root of the confining pressure; this result agrees qualitatively with field observations and the results of sand-box experiments and quantitatively with direct measurement of dilatancy during high-pressure rock-deformation experiments.

INTRODUCTION

IT IS commonly postulated that, in the brittle domain, crustal rocks obey the Coulomb–Navier failure criterion (Coulomb 1773). The application of the Coulomb–Navier criterion has apparently been very successful in predicting fault patterns observed in the field and in scaled experiments on analogue materials such as dry sand or clay (Riedel 1929). The Coulomb–Navier criterion predicts that, at failure, there is a linear relationship between the normal and shear stresses acting across the plane of failure. From such a linear relationship very simple and attractive geometrical arguments have been derived relating the geometry of the plane of failure to the directions of the principal stresses. However, it has often been noted that the results of deformation experiments on rock samples cannot be fitted by a simple linear relationship such as the Coulomb–Navier criterion (Murrell 1965, Paterson 1978). This seems to indicate that the Coulomb–Navier criterion may be an over-simplification of the real brittle behaviour of crustal rocks that is only valid under specific stress conditions such as those characteristic of the near surface. Furthermore, because the criterion depends on the value and orientation of the principal stresses, it is rather difficult to test in the field. In fact, the criterion is often used to constrain the geometry of the regional stress field from fault orientations rather than vice versa. There is therefore a need for further developing and testing of rheological models for the Earth's brittle crust.

Scaled laboratory experiments on analog materials such as dry sand or clay have been used to develop and constrain mechanical models (Riedel 1929, Horsfield 1977, Naylor *et al.* 1986, Richard & Cobbold 1989). Some rock properties such as cohesion or elasticity cannot however be properly scaled to the finite dimensions of the laboratory. Moreover, as in natural examples of crustal deformation, the nature of the stress field within the deforming sample is rather difficult to determine especially following finite strains and displacements.

Numerical analyses have also been used successfully to reproduce the large scale features of crustal deformation from which mechanical considerations have been derived (Braun & Beaumont 1987, Bassi 1991, Chéry *et al.* 1991). Numerical models offer the attractive benefit of providing a complete picture of the stress and strain fields within the deforming body. Unfortunately, numerical modelling of the Earth's crust has been limited so far by the approximations of two-dimensionality and/or infinitesimal deformations.

In this paper, we present the results of a complex three-dimensional finite element model of the brittle crust based on Murrell's extension in three dimensions of Griffith's failure criterion. The model is used to perform a series of finite deformation experiments at the crustal scale, the results of which are compared to field and laboratory observations to test the applicability of Murrell's criterion to the brittle behaviour of crustal rocks.

Wrench tectonics offers a natural laboratory in which models of the crust's rheological behaviour may be easily tested. Indeed, past and present-day examples of strike-slip faults or terranes are numerous and have been extensively studied. Moreover, because strike-slip deformation usually does not result in substantial vertical

movement of the surface, structures formed by horizontal shearing of the Earth's crust are little affected by erosion or sedimentation and are therefore readily observable. Unfortunately, due to its fundamental three-dimensional nature, strike-slip deformation cannot be properly addressed under the assumption of two-dimensionality.

In the paper, we first describe the 'classical' theory of wrench faulting based on the Coulomb–Navier failure criterion. We then compare it to predictions based on Murrell's criterion under uniform shear stress conditions. A series of numerical experiments performed with the finite element model are then analysed in the light of the results of the simplified stress analysis. Results from laboratory experiments and field observations are also used to test the numerical model predictions.

FAULT PATTERNS UNDER UNIFORM STRESS CONDITIONS

In a material obeying the Coulomb–Navier fracture criterion, failure takes place on a plane when the shear stress acting on that plane, τ, attains the value (Coulomb 1773):

$$|\tau| = S_0 - \mu\sigma, \tag{1}$$

where S_0 is the inherent shear strength of the rock, μ the coefficient of internal friction and σ the normal stress acting on the plane. By convention, tensile stresses are positive.

The state of stress in a region of the crust subjected to a uniform horizontal shear stress, σ_0 (Fig. 1a) is:

$$\begin{aligned} \sigma_{xx} &= \sigma_{yy} = \sigma_{zz} = -\rho \mathbf{g} z \\ \sigma_{xy} &= \sigma_0; \sigma_{yz} = \sigma_{zx} = 0, \end{aligned} \tag{2}$$

where ρ is the density of the crust and z is measured from the surface, positive downwards. The corresponding normal and shear stresses on a plane whose normal is defined by the angles (ϕ,θ) (defined in Fig. 1b) are given by:

$$\begin{aligned} \sigma &= -\rho \mathbf{g} z + \sigma_0 \sin 2\phi \sin^2\theta \\ \tau &= \sigma_0 \cos 2\phi \sin\theta. \end{aligned} \tag{3}$$

The principal stresses are given by:

$$\begin{aligned} \sigma_1 &= -\rho \mathbf{g} z + \sigma_0 \\ \sigma_2 &= -\rho \mathbf{g} z \\ \sigma_3 &= -\rho \mathbf{g} z - \sigma_0 \end{aligned} \tag{4}$$

and their orientations are shown in Fig. 1(a).

Introducing equation (3) into equation (1), we obtain the following relationship:

$$\sigma_0 = \frac{S_0 + \mu\rho \mathbf{g} z}{\sin\theta[\pm\cos 2\phi + \mu \sin 2\phi \sin\theta]}, \tag{5}$$

the minimum value of which takes place at angles:

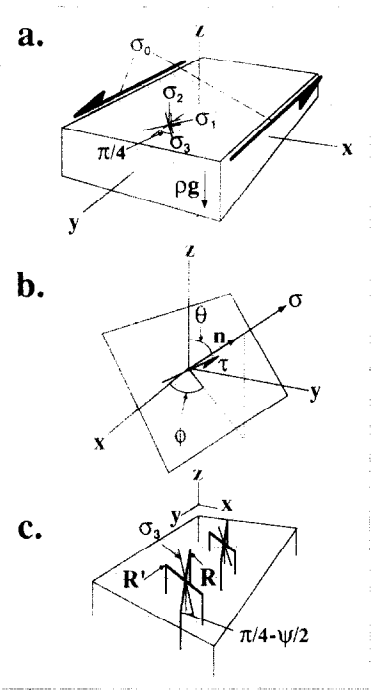

Fig. 1. (a) Principal stress (σ_1, σ_2, σ_3) orientations in a crustal block under strike-slip stress conditions. (b) The angles ϕ and θ are used to define the direction of the normal, **n**, to a plane. σ and τ are the stress components in a direction normal and tangential to the plane, respectively. (c) Orientation of the Riedel shears R and R' in a material obeying the Coulomb–Navier failure criterion with respect to the direction of the most compressive principal stress, σ_3.

$$\theta = \frac{\pi}{2}; \qquad \phi = \frac{\pi}{4} \pm \left(\frac{\pi}{4} - \frac{\psi}{2}\right), \tag{6}$$

where ψ is the angle of internal friction defined by:

$$\tan\psi = \mu. \tag{7}$$

Shearing should therefore be initiated along vertical faults oriented at angles $\pm(\pi/4 - \psi/2)$ with respect to the direction of the greatest compressive stress, σ_3, and this irrespective of the inherent shear strength, S_0, and the depth (Fig. 1c).

In shear experiments, the geometry of these potential Coulomb faults was first reproduced by Riedel (1929) in a wet clay cake. They therefore carry the name of Riedel shears. Those forming the smallest angle with the direction of shear (the y-direction) are called synthetic or R-shears; those that form the smallest angle with the x-direction are called antithetic or R'-shears. The theory has also been used to explain the geometry of surface faulting in tectonic shear zones (see, for example, McMahon Moore 1979).

The simple Coulomb–Navier criterion predicts that the orientation of the Riedel shears is independent of the gravitational hydrostatic stress and therefore should remain planar throughout the entire brittle crust. It is, however, a well known fact (Harding 1985, Naylor *et al.* 1986, Richard & Cobbold 1989) that the synthetic Riedel shears tend to rotate with increasing depth and to align themselves with the direction of shearing (that is at 45° to the horizontal principal stresses) to form so-called 'flower' structures (Fig. 2a). It has been suggested that,

at some depth within the crust, there exists a boundary between two rigid blocks that are sliding one against the other (Fig. 2b). The shearing between the two blocks is transferred to the overlying brittle crust. Close to the rigid blocks, the shearing is limited to a narrow zone aligned with the strike of the boundary between the two blocks; further away from the blocks, deformation takes place on a wider scale and Riedel shears are allowed to develop at angles determined by the angle of internal friction of the material according to equation (6).

This model is based on the hypothesis that there exists somewhere in or just below the crust a layer where the Coulomb–Navier criterion does not hold (the crystalline basement beneath a sedimentary basin, a mid-crustal 'strong' layer or the uppermost mantle?). Although we do not dispute the physical plausibility of the 'rigid block model', we wish to propose an alternate, more natural explanation for the formation of flower structures based on an alternative criterion for the inception of rock failure.

Extending the work of Griffith (1921) to three dimensional stress distributions, Murrell (1963) suggested the following criterion for rock failure expressed in terms of the principal stresses:

$$(\sigma_1 - \sigma_2)^2 + (\sigma_2 - \sigma_3)^2 + (\sigma_3 - \sigma_1)^2 + 24T_0(\sigma_1 + \sigma_2 + \sigma_3) = 0, \quad (8a)$$

where T_0 is a material property called the tensile strength. In principal stress space, this criterion is represented by a paraboloid of revolution around the pressure (or hydrostatic) axis. Note that the relationship (8a)

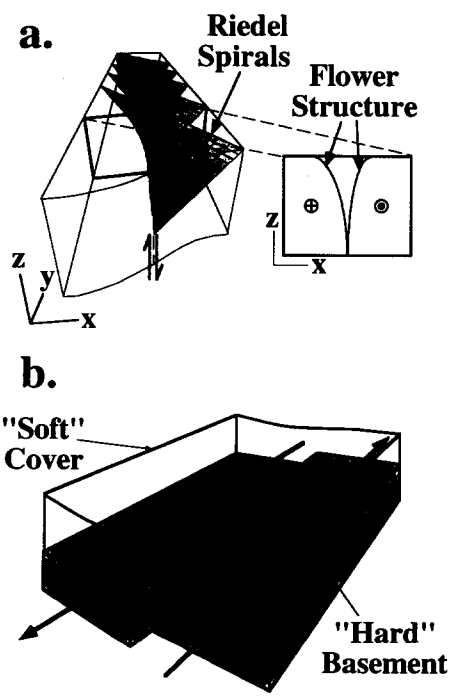

Fig. 2. (a) Schematic representation of spiral Riedel shears as observed in scaled laboratory experiments and their possible interpretations in terms of 'flower' structures observed along vertical seismic reflection profiles. (b) The 'basement wrench' model in which two rigid basement blocks slide pass each other resulting in a more diffuse deformation in the overlying softer sedimentary cover.

breaks down for tensile principal stresses and it must be replaced by one of the following equalities:

$$\sigma_1 = T_0;\ \sigma_2 = T_0;\ \sigma_3 = T_0. \quad (8b)$$

In the special range of stress states for which

$$\sigma_2 = \frac{\sigma_1 + \sigma_3}{2}, \quad (9)$$

Murrell (1963) showed that the criterion may be expressed in terms of the normal (σ) and tangential (τ) stresses on a reference plane in the following way:

$$\tau^2 + 12T_0\sigma = 36T_0. \quad (10)$$

This relationship corresponds to a parabola in the $[\sigma,\tau]$ Mohr space.

Mohr's criterion for incipient fault orientation states that faults will develop preferentially along surfaces the normal of which makes an angle β with the most tensile principal stress, σ_1, satisfying the following relationship in the $[\sigma,\tau]$ space:

$$\frac{\partial\tau}{\partial\sigma} = -\cot 2\beta. \quad (11)$$

Combining equations (10) and (11) leads to:

$$\cos^2 2\beta = \frac{36T_0^2}{\tau^2 + 36T_0^2}. \quad (12)$$

From equations (8) and (9), we may deduce that, at failure, the following relationship applies between the maximum and minimum principal stresses:

$$(\sigma_1 - \sigma_3)^2 + 24T_0(\sigma_1 + \sigma_3) = 0. \quad (13)$$

Combining equations (12) and (13) and after some algebra, one finally obtains:

$$\cos 2\beta = -\frac{1}{2}\frac{\sigma_1 - \sigma_3}{\sigma_1 + \sigma_3}. \quad (14)$$

The same expression was derived by Murrell (1958) based on the two-dimensional version of (8). In a crust under shear, equation (4) combines with equation (14) to yield:

$$\cos 2\beta = \frac{1}{2}\sqrt{\frac{3}{\Psi}}, \quad (15)$$

where

$$\Psi = \frac{\rho g z}{4T_0}.$$

Note that equation (15) is only valid if $\Psi \geq 3/4$; in cases where $\Psi < 3/4$, equation (15) should be replaced by $\cos 2\beta = 1$.

Close to the surface ($\Psi = 3/4$), the Riedel shears have degenerated into a single fault plane parallel to the direction of the most compressive stress (σ_3). As depth (and overburden thickness) increases, a system of two Riedel shears develop one on either side of the direction of the most compressive stress. For large values of Ψ, the Riedel shears are orthogonal and the synthetic (or main)

shear is practically aligned with the direction of the applied shear stress, σ_0. It is therefore a 'natural' behaviour of a crust behaving according to Murrell's criterion to form deep crustal boundaries that slide against each other from which spiral-like Riedel shear planes radiate towards the surface to form flower structures. Note that the height of the flower structures is proportional to the strength of the material; in other words, Riedel spirals may form in a relatively thin 'weak' sedimentary covers but may also extend through the 'harder' crust to depths of several tens of kilometers, possibly down to the Moho.

So far we have only dealt with the formation of faults under uniform stress conditions. As deformation accumulates on this first set of faults, one may expect (a) re-organization of the stress field and (b) translation and rotation of the faults themselves. According to the Coulomb–Navier criterion, subsequent faulting should therefore take place at an angle $\pi/4 - \psi/2$ with respect to the new σ_3 orientation to form so-called *P* shears (Naylor *et al.* 1986). Note that, because the perturbed state of stress is in most practical situations unconstrained, such a reasoning permits us to call any secondary fault a '*P*-shear' regardless of its orientation. Also based on the Coulomb–Navier failure criterion, Nur *et al.* (1986) remarked that rigid block rotation in a region undergoing finite shearing induces rotation of the initial Riedel shears with respect to the slip direction in such a way that a new set of Riedel shears will form cutting through the first set at an angle between 25° and 45°. The predictions appear to be supported by field evidence (Nur *et al.* 1989).

In a material obeying Murrell's failure criterion, to predict the orientation of secondary Riedel shears is a more complex problem that requires not only a knowledge of the evolution of the principal stress orientation but also of the relative amplitude of the principal stresses following finite deformation (cf. equation 14).

THE NUMERICAL MODEL

The previous section described the theoretical behaviour of the brittle crust under an ideal uniform stress state. We wish now to solve the problem of brittle crustal deformation in three dimensions under more general conditions, that is following imposed forces or displacements along specified boundaries. This requires us to determine the state of stress within a given volume of the crust by solving the equations of force and moment equilibrium. The deformations (or strains) should then be related to the stresses via a rheological law.

To solve the equations of force and moment equilibrium (Fung 1965), we use the finite element method (Zienkiewicz 1977). We elected to use 20-node quadratic parallelepiped elements and a 27-point Gauss integration scheme.

The crust is regarded as an elasto-plastic material characterized by two elastic constants E (Young's modulus) and ν (Poisson's ratio) and a yield strength, T_0. The material behaves elastically unless the state of stress lies outside of the yield envelope defined by Murrell's failure criterion (equation 8). The criterion may be expressed in a simpler form in terms of stress invariants:

$$F = J_{2D} + 12T_0 p = 0, \qquad (16)$$

where J_{2D} is the second invariant of the deviatoric part of the stress tensor and p the pressure. If the predicted elastic stress state lies outside of the yield envelope, we use the radial-return algorithm of Wilkins (1963) to compute the new stress configuration (see Appendix 1). Beyond yield, the material deforms plastically according to an associative plastic flow law (Owen & Hinton 1980) in which the plastic strain increment is assumed to be normal to the yield envelope.

The elasto-plastic rheology is used as an analog to the brittle deformation of the upper crust that results from macro- and micro-fracturing of rock units as well as the more 'ductile' intra-grain plasticity (Paterson 1978). It is important to note here that we use the term 'plasticity' in the sense of the engineers, that is a non-linear time- and temperature-independent mode of deformation.

To handle properly finite incremental deformation in the Lagrangian formulation, we make use of the mid-point incremental strain and the Green–Naghdi stress rate (Hughes & Winget 1980) (see Appendix 2).

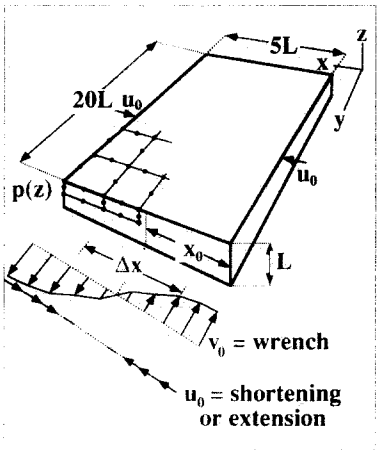

Fig. 3. The finite-element model set-up. Deformation is driven by imposed displacements at the base of the crustal block (v_0 and u_0) and along its sides (u_0). The finite-element mesh is made of 5000 elements connecting 69,576 degrees of freedom. The components of the stress, strain and rotation tensors are calculated at 135,000 integration points.

EXPERIMENTAL SET-UP

Several experiments have been performed with the numerical model. They all share the following set-up. A piece of crust of thickness L, length $20L$ and width $5L$ is subjected to a left-lateral wrench imposed along its rigid base (Fig. 3). The incremental displacements (u, v, w) along the bottom boundary are imposed in the following way:

$$u = 0$$

$$v = v_0 \frac{2}{\pi} \arctan\left(\frac{x - x_0}{\Delta x}\right) \quad (17)$$

$$w = 0,$$

where $x_0 = 5L/2$ and Δx is the width over which the wrenching is taking place. Δx varies between model runs. Note that following the theoretical developments above, such a basal boundary condition is a 'natural' one in that it respects the mechanical behaviour of the material at high pressure.

In some model runs, in addition to wrenching, the crustal block also experiences shortening or extension driven by its base in a direction normal to the direction of the shear:

$$u = u_0 \frac{2}{\pi} \arctan\left(\frac{x - x_0}{\Delta x}\right). \quad (18)$$

We introduce here the parameter r, defined as the ratio between the imposed tangential and normal incremental displacements:

$$r = \frac{u_0}{v_0}. \quad (19)$$

The side boundaries at $x = 0$ and $x = 5L$ are characterized by a fixed normal displacement ($u = u_0$); whereas the side boundaries at $y = 0$ and $y = 20L$ are free boundaries on which a normal 'containment' pressure is imposed:

$$p(z) = \rho \mathbf{g}(z - L), \quad (20)$$

where z is measured from the base of the model, positive upwards. This pressure ensures that the material does not spread out under its own weight. This set-up is conceptually equivalent to plunging the model crust in an inviscid fluid of similar density.

The crust is also subjected to gravitational forces proportional to the density of the material, ρ.

Two important dimensionless numbers must be defined: (a) the ratio of plastic to elastic 'strengths': $4T_0/E$, assumed constant in all model runs ($4T_0/E = 8 \times 10^{-4}$); and (b) the ratio of gravitational stresses to the plastic strength: $\rho \mathbf{g} L/4T_0$. This latter dimensionless quantity is referred to as the plastic Argand number, Ar^P, and will vary amongst the model runs. Assuming that the plastic strength and density of the crust are known quantities (≈ 20 MPa and 3000 kg m^{-3}, respectively), variations in Ar^P correspond to variations in the assumed crustal block thickness.

THE MODEL RESULTS

The reference run

The parameter values characterizing the model runs are given in Table 1. The first run, which we will call the 'reference' run, is characterized by basal wrenching only (no contraction or extension), an Argand number characteristic of a 30 km thick crustal block and a narrow zone of basal shear. The model was run for 11 steps leading to a total tangential displacement of L between the two far rigid walls or an averaged shear strain of $L/5L = 20\%$. The first step in all model runs is a 'settling' step during which the crustal block compacts in response to gravitational forces alone; the basal and side velocity boundary conditions are turned on at the beginning of the second time step only.

Table 1. Values of the plastic Argand number (Ar^P), the width of the basal wrenching (Δx) and the ratio of normal to wrench displacement (r) for the seven model runs

Run	Ar^P	Δx	r
1	11.25	0.02	0.
2	11.25	0.05	0.
3	5.625	0.02	0.
4	11.25	0.02	−0.1
5	11.25	0.02	−0.3
6	11.25	0.02	0.1
7	11.25	0.02	0.3

The results of the computation are shown in Fig. 4 as contours of the incremental xy-shear strain ($\Delta\varepsilon_{xy}$) along a horizontal plane close to the surface ($y = 0.97L$). At first (Fig. 4a), a narrow vertical zone of intense shear develops above the basement wrench. As deformation progresses (Figs. 4b–e), the zone of deformation widens, and a series of 'en échelon' Riedel-like zones develop making an increasingly large angle (γ) with the y-direction. From time step 6 onwards (Figs. 4f–h), the Riedel shears are formed at a constant angle γ and are partially abandoned in favour of two thin regions of intense shear aligned with the direction of wrenching (Y-shears). During the last two time steps (Figs. 4i&j), the Riedel shears become sigmoidal as a ridge of non-deforming material develops along the central region of the model (the white areas).

We chose to display the results of the computations by means of contour plots of $\Delta\varepsilon_{xy}$, the horizontal shear strain increment. Strain in the field or in the laboratory is measured along the strike of the various shear zones. To do this in our computations would require computation of $\Delta\varepsilon_{x'y'}$, where x' and y' are orthogonal directions aligned at $\pm\pi/4$ angles with respect to the strike of a local ridge (or maximum) in $\Delta\varepsilon_{x'y'}$. In other words, the component of the strain tensor to contour should be a function of the local value of the strain tensor. This is a very complex inverse problem which we avoided by contouring $\Delta\varepsilon_{xy}$ everywhere. The main drawback of our choice is that shear zones inclined at $\pm\pi/4$ with respect to the x-axis are not visible in contour plots of $\Delta\varepsilon_{xy}$.

Figure 5 shows horizontal contours of the shear strain increment for one particular time (end of time step 8) but at different depths. As depth increases, the sheared region between the two bounding faults narrows and the angle (γ) that the Riedel shears make with the y-direction rapidly decreases. At a depth of $0.80L$, the Y-shears on either side of the deformed region are abandoned in favour of the Riedel shears. The Riedel shears have become parallel to the y-axis at a depth of approximately $0.6L$.

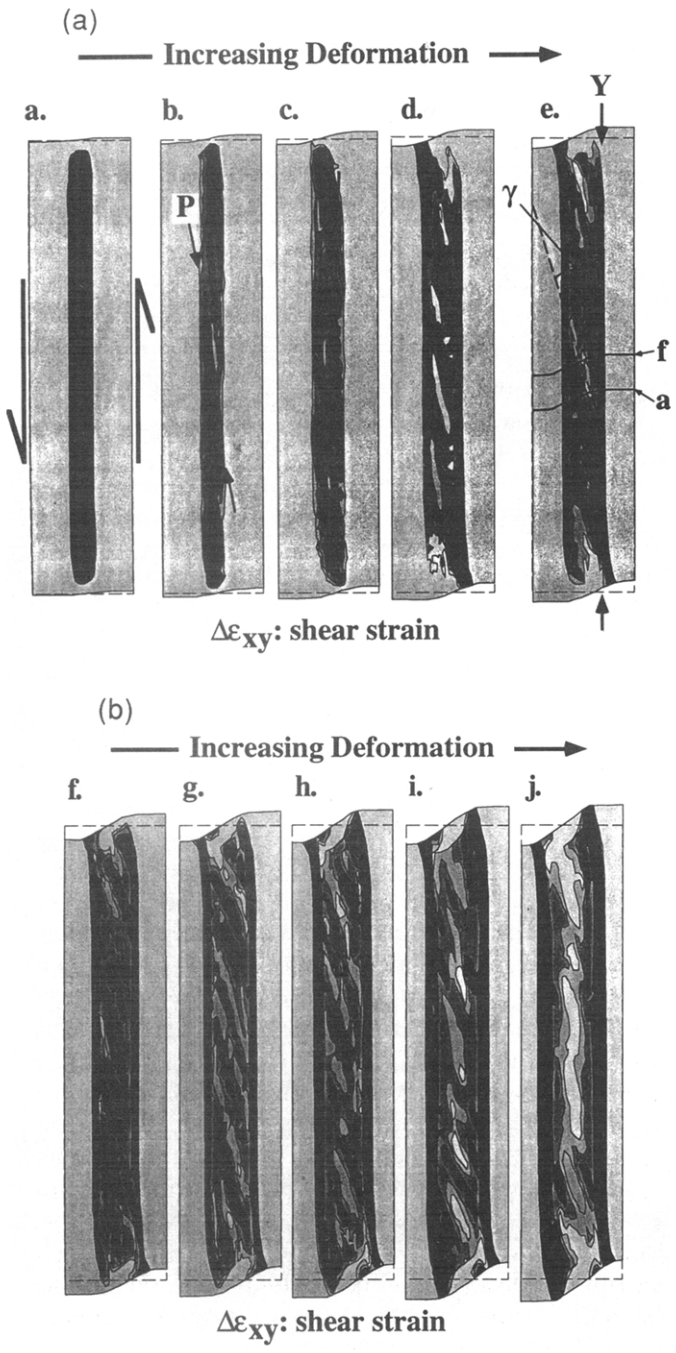

Fig. 4. Contours of the incremental horizontal shear strain, $\Delta\varepsilon_{xy}$, along a horizontal cross-section at the surface of the finite-element mesh for time steps 2–11 (a–j) for the reference model run. The darkest areas are regions of maximum incremental strain (> 8%); the lightest areas are regions of minimum incremental strain (< 3%). The orientation of a particular *P*- and *Y*-shear is indicated on panels (b) and (e). The angle γ is defined in panel (e) as well as the location of the vertical cross-sections shown in Figs. 6(a)–(f).

Figure 6 shows contours of the horizontal incremental shear along a series of vertical cross-sections oriented perpendicular to the direction of shearing (the *y*-axis) for time step 6. The model predicts the formation of a well-defined zone of intense deformation rooting into the region of imposed shear along the basal boundary and opening out upwards in a 'flower-like' structure (Harding 1985). The Riedel shears (thick dashed lines in Fig. 6) form spiral-like planes.

Comparison with simplified stress analysis

The numerical model predicts that the first structure to develop is a zone of diffuse *Y*-shear. This is quite contrary to the predictions of the simplified stress analysis developed in the second paragraph and summarized in equation (15). The main reason for this apparent incompatibility is that, in the finite element model, the initial stress and strain distributions are controlled by the elastic properties of the material and the geometry and nature of the boundary conditions.

As a result, the stress distribution prior to failure is rather different from the one assumed in equation (4). Figure 7(a) shows the horizontal shear stress distribution after a moderate amount of shear assuming that the material behaves in a pure linear elastic fashion. The condition of uniform shear stress, σ_0, assumed in the stress analysis (equation 4) is only valid in the central region of the model overlying the boundary where the displacement is imposed. Following increased deformation, plastic failure takes place where elastic stress, and thus strain, had previously built up: Figs. 7(a) & (b) show the horizontal shear strain distribution in the modeled crust in the purely elastic case and elastic–plastic case, respectively. The plastic deformation appears to have inherited the character of the elastic solution. It is therefore a result of the elastic component of the assumed rheology and the geometry of the boundary conditions that a narrow, elongated shear zone develops at first. One could also argue that the *Y*-shears are the 'kinematically preferable' mode of shear deformation in that they minimize the volume over which deformation takes place.

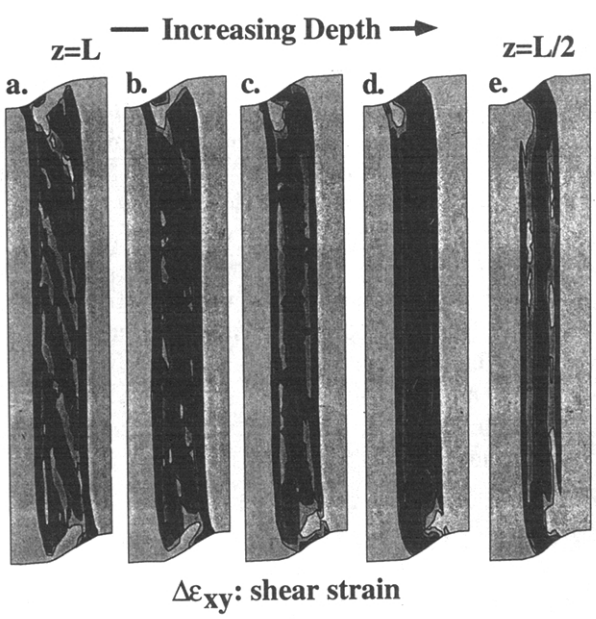

Fig. 5. Contours of the incremental horizontal shear strain, $\Delta\varepsilon_{xy}$, along several horizontal cross-sections at different depths through the crust at time step 6 for the reference model run. The depths are *L*, 4*L*/24, 7*L*/24, 10*L*/24 and *L*/2 in panels (a), (b), (c), (d) and (e), respectively. Note that the contour values are not the same for all panels but, rather, were chosen to highlight the orientation of the *P*- and *Y*-shears at each depth.

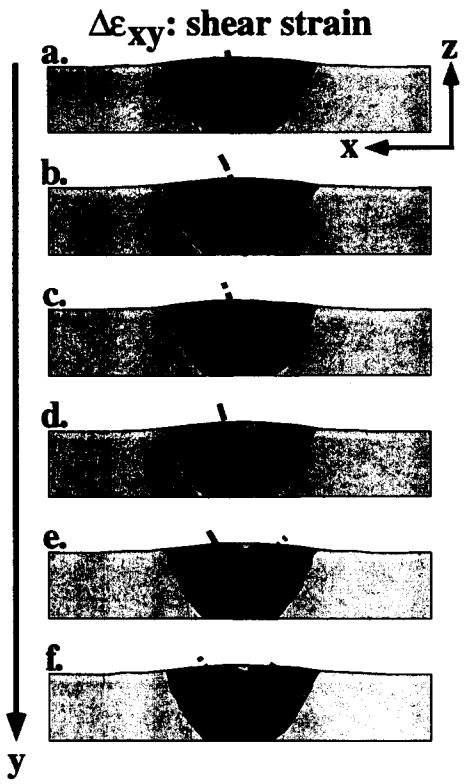

Fig. 6. Contours of the incremental horizontal shear strain, $\Delta\varepsilon_{xy}$, along several vertical cross-sections located between cross-sections a and f shown on Fig. 4(e) at time step 6 for the reference model run. The darkest areas are regions of maximum strain (> 11%); the lightest areas are regions of minimum strain (< 5%).

As plastic deformation accumulates, the orientation of the Riedel shears evolves with increasing deformation and depth, at least qualitatively in agreement with the stress analysis: the Riedel shears appear to rotate counter-clockwise (Figs. 4b–j) with increased deformation and, at any given time, the shear zones tend to rotate with increasing depth in a clockwise manner to form a series of spirals (Figs. 5a–e).

If the oblique shear zones were 'true' Riedel shears, one would expect them to be aligned with the most compressive principal stress, σ_3, at the surface and rapidly rotate with increasing depth to become parallel to y-axis. In fact, the oblique shear zones predicted by the numerical model are degenerate Riedel shears or P-shears in the sense that their orientation with respect to

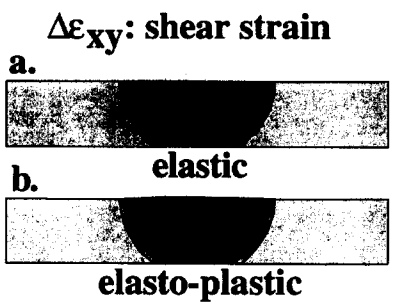

Fig. 7. Contours of the incremental horizontal shear strain $\Delta\varepsilon_{xy}$, along a vertical cross-section halfway between the two side boundaries (at $y = 10L$) at time step 2, (a) assuming a perfectly elastic rheology and (b) assuming an elasto-plastic rheology based on Murrell's failure criterion.

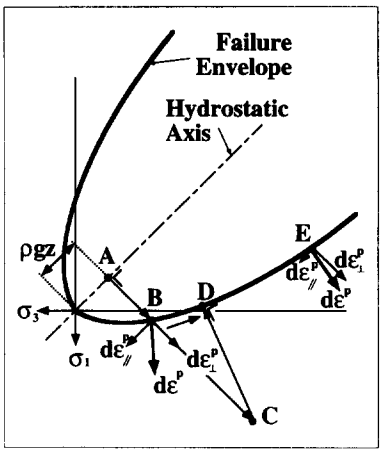

Fig. 8. The evolution of the stress state in the $[\sigma_1, \sigma_3]$ space following the application of a shear stress, σ_0, on a material point initially under hydrostatic stress condition at point A. B is the elastic/plastic stress limit and D is the stress configuration following finite plastic deformation. Also shown are the components of the plastic strain increment parallel and normal to the pressure axis ($d\varepsilon_{\parallel}$ and $d\varepsilon_{\perp}$, respectively) at locations B and E.

the principal stress axes behaves according to equation (14) but not to equation (15). That their orientation does not obey (15) results from the rapid change of the principal stress magnitude following finite plastic deformation.

Figure 8 shows schematically the evolution of the horizontal principal stresses, σ_1 and σ_3, following deformation. At a given pressure (point A), determined by the weight of the overburden, the imposed wrenching drives the stress state towards the failure envelope (point B) by contributing equally to both horizontal principal stresses but positively along the σ_1-axis and negatively along the σ_3-axis. At failure, the stress state is such that equation (15) is valid and faulting should take place along properly orientated Riedel shears. Following plastic flow, the stress state migrates along the failure envelope to reach a stable configuration that is given by the normal projection of the elastic stress state (point C) onto the failure envelope (point D) (Wilkins 1963). This 'wandering' in the stress space involves a modification of the amplitude of σ_1 and σ_3 without affecting the principal stress directions. In a material obeying the Coulomb–Navier plastic criterion, this stress migration would not influence the orientation of the Riedel shears but in a material behaving according to Murrell's failure criterion, the stress redistribution induces rotation of the Riedel shears according to equation (14).

This point is illustrated in Table 2 where the orientations of the shear bands as they appear in the computations is compared with the theoretical values predicted by equation (14) from the computed principal stress values and orientations. Qualitatively, the results agree: during the first six time steps, the Riedel shears rotate counterclockwise in accordance with the principal stress orientation and magnitude (via relation 14); in the later stages of deformation, the Riedel shears form at a constant angle with respect to the y-axis ($\gamma \approx 20°$). That the computed orientations do not perfectly match the

predictions is due to the fact that relationship (9) between the three principal stress components on which (14) is based is not always valid.

In conclusion, one may state that the orientation of the Riedel shears during finite deformation is rather different from that predicted by a simple stress balance argument. Modification of the stress state following plastic deformation has important implications for the orientation of those Riedel shears that are going to take up most of the finite deformation. This argument may be regarded as a generalization of the 'stress re-orientation' of Naylor *et al.* (1986) following finite deformation on a primary set of Riedel shears leading to the formation of secondary *P*-shears.

Comparison with observations

The results of the computation corroborate the observations of Bartlett *et al.* (1981) from wrench experiments on limestone at varying confining pressures: (1) after finite deformation, most of the displacement is taken by *Y* shears orientated parallel to the strike of the basement fault; (2) Riedel shears form on either sides of the *Y* shears but can accommodate only a small fraction of the total displacement; and (3) in cross-section, the shear zone is wedge-shaped, its width increasing with accumulated displacement.

A major difference between the results obtained in most analog experiments is that our model results do not reproduce the so-called '*R*'-shears. Rather, in the early stages of the computations, a region of diffuse deformation aligned with the *y*-direction develops. The reason for this apparent discrepancy is the elastic component built into our mechanical model that forces shearing aligned with the *y*-axis to dominate in the early stages of the 'experiments'; it is only later, when plastic deformation becomes substantial, that *P*-shears appear, oriented with respect to the stress tensor in accordance with Mohr's incipient failure criterion.

Finally, the 'long-term' or 'steady-state' solution obtained from the computations shows strong resemblance to field examples of shear zones where most of the slip is taken up by one or several faults aligned with the direction of shearing (*Y*-shears) connected to each other by oblique sub-faults to form so-called 'duplexes' (Woodcock & Fischer 1986). Examples are shown in fig. 2 of Woodcock & Fischer (1986).

Dilatancy

The results of the computation also show that the surface overlying the region between the two bounding faults bulges upwards (Fig. 6). As none of the lateral boundaries experiences a normal displacement and as the bottom boundary is forced to remain flat at all times, the surface uplift indicates that the finite shear deformation induces dilatation (or volume increase). In Fig. 9(a), a vertical cross-section of the modelled crust is shown in which the trace of the incremental strain tensor (i.e. incremental volume change) has been contoured. The increase in volume is confined to the region between the two bounding faults nearest to the surface.

To understand the origin of the dilatation, we must go back to the associative plastic flow law used in the numerical model that assumes that the plastic strain increment is normal to the failure envelope. The direction of the strain increment, $d\varepsilon^P$, is shown in Fig. 8 for two points on the failure envelope (B and E) as well as its components parallel ($d\varepsilon^P_{\parallel}$) and normal ($d\varepsilon^P_{\perp}$) to the pressure axis. Note that the ratio of plastic dilatation to isochoric deformation (also called dilatancy) is proportional to the ratio $d\varepsilon^P_{\parallel}/d\varepsilon^P_{\perp}$. Close to the summit of the parabola (point B), this ratio is relatively large, but as pressure increases, dilatancy decreases to rapidly become negligible (point E).

It therefore appears that the combination of Murrell's failure criterion with an associative plastic flow law leads to plastic dilatancy inversely proportional to the confining pressure. The question arises as to whether this 'mathematical' behaviour bears any resemblance with the true mechanical behaviour of crustal rocks. In other words, should we use an associative plastic flow law to

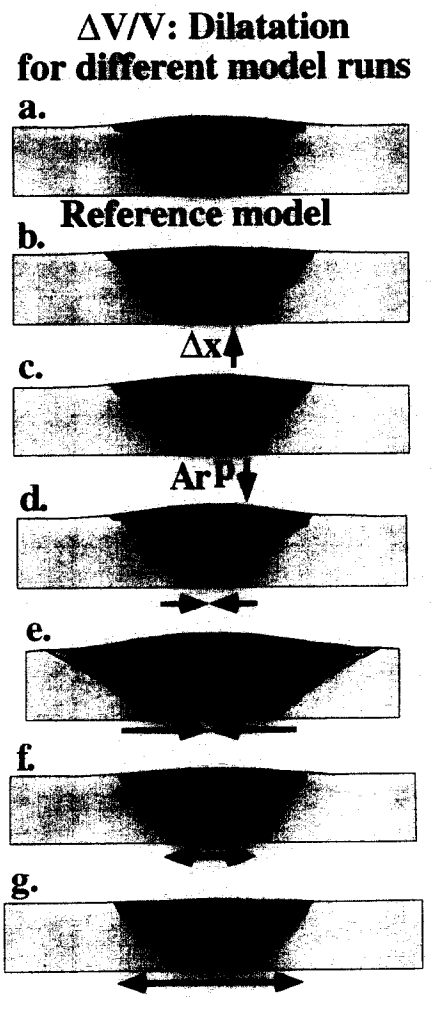

Fig. 9. Contours of the incremental volume change ($\Delta V/V$) along a vertical cross-section halfway between the two side boundaries (at $y = 10L$) at time step 6: panels (a)–(g) correspond to model runs 1–7, respectively. The darkest areas are regions of maximum volume change (> 0.7%); the lightest areas are regions of minimum volume change (< 0.3%).

Table 2. Values of γ, the angle made by the Riedel shears with the y-axis, for the different time steps of the reference model run. The various columns correspond to the values of γ: (1) measured from the strain field at the surface; (2) deduced from the stress field at the surface; (3) measured from the strain field at the base of the crust; and (4) deduced from the stress field at the base of the crust

Step	(1) Surface-observed	(2) Surface-deduced	(3) Base-observed	(4) Base-deduced
2	0°	12°	0°	4°
3	7°	20°	0°	8°
4	9°	22°	0°	9°
5	16°	23°	0°	9°
6	18°	21°	0°	8°
7	17°	23°	0°	8°
8	18°	22°	0°	7°
9	17°	22°	0°	6°
10	?	21°	0°	6°
11	?	22°	0°	5°

represent the brittle deformation of rocks the strength of which is known to increase dramatically with confining pressure?

To answer that question, let us first quantify dilatancy in a material failing according to Murrell's criterion. Following the associative plastic flow law, the plastic strain increment, $d\varepsilon^P$, is normal to the failure envelope:

$$d\varepsilon^P = \lambda \frac{\partial F}{\partial \sigma},$$

where λ is a scalar function of the stress state; the trace of the plastic strain increment is a measure of plastic volume change:

$$\text{trace}\,(d\varepsilon^P) = \frac{\Delta V^P}{V} = 12T_o\lambda,$$

and the second invariant of its deviatoric part, E^P_{2D}, may be expressed in the following manner:

$$E^P_{2D} = \lambda^2 J_{2D} = -12T_0 p\lambda^2.$$

Dilatancy is defined as:

$$\frac{\dfrac{\Delta V^P}{V}}{\sqrt{E^P_{2D}}} = \sqrt{\frac{-12T_0}{p}}. \qquad (21)$$

Murrell's theory therefore predicts that dilatancy is inversely proportional to the square root of the pressure. Qualitatively, this seems reasonable (Mandl 1988, p. 322). Note, however, that the dilatancy does not require plastic work (see Appendix 3).

This inverse relationship between dilatancy and confining pressure has been observed in laboratory experiments on Carrara marble (Scholz 1968, Edmond & Paterson 1972, Zhang 1992). During wrenching experiments on limestone, Bartlett *et al.* (1981) observed upthrust of material within the wedge-shaped shear zone inversely proportional to the confining pressure. Direct measurements of crustal deformation in active wrench systems also tend to indicate that substantial volume changes accompany strike-slip deformation (Raleigh & Burford 1969, Burford *et al.* 1972).

PLAYING WITH THE PARAMETERS

Shearing above a wide zone of basal wrenching

In the second run, the width of the region of imposed wrenching (Δx) along the base of the modelled crust has been doubled (Table 1). This apparently minor modification in the basal boundary condition leads to a profound change in the structures that form within the overlying crust. The single initial shear zone that evolves into a system of twin thin shear zones connected by oblique Riedel shears (Fig. 10a) is replaced by a single shear zone breaking up into segments that rotate to form an array of Riedels (Fig. 10b). The zone of deformation is more diffuse and is not bounded by well-defined Y-shears.

This result is in good agreement with the variations in structural style observed in laboratory experiments where a pile of sand or clay is subjected to a basal shear. In situations where the imposed shear is distributed over a wide zone (Wilcox *et al.* 1973), long overlapping Riedel shears develop and can accommodate substantial deformation. In situations where the deformation is imposed across a single basement fault (Naylor *et al.* 1986), shorter Riedels develop in a narrow zone overlying the fault. These Riedels can accommodate very small amounts of deformation and new Riedels develop very rapidly.

In vertical cross-section, the wedge-shaped zone of deformation is characterized by a larger number of spiral-like Riedel shears (Fig. 11b) in comparison with run 1 (Fig. 11a). Also the zone of maximum shear strain at the base of the model is wider and reflects the geometry of the basal boundary condition.

In general terms, one could state that the greater width of the imposed wrench at the base of the model permits the natural (or dynamical) structures, the P-shears, to take up a greater proportion of the overall deformation to the detriment of the forced (or kinematic) structures, the Y-shears. By dynamical structures we mean those that form in accordance with the stress distribution and the mechanical properties of the material; kinematic structures are those that form in

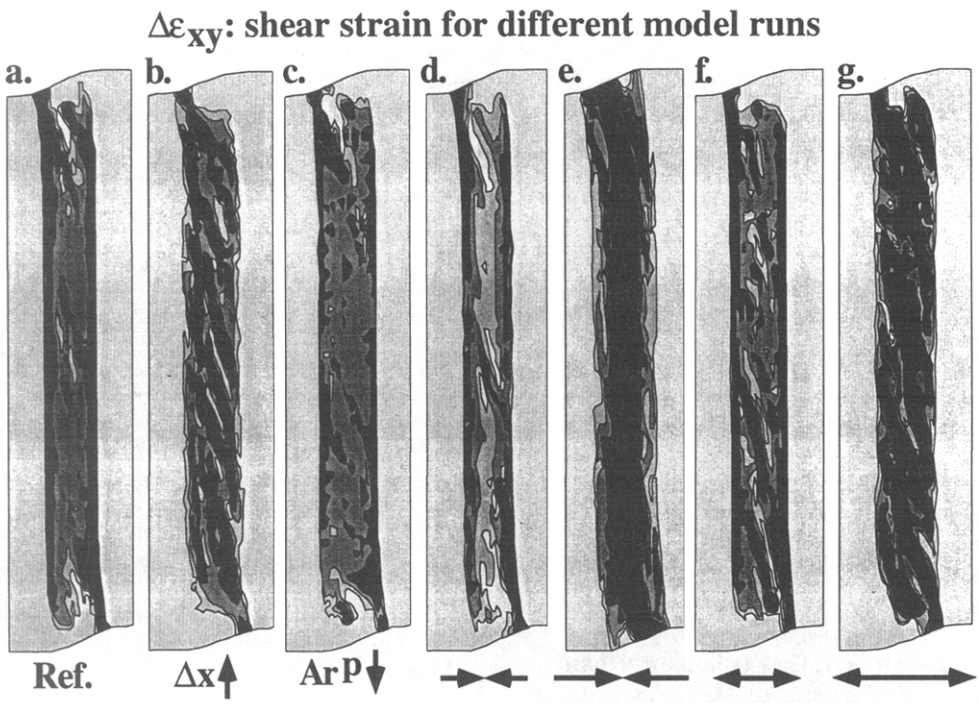

Fig. 10. Comparison between different model runs of the incremental horizontal strain ($\Delta\varepsilon_{xy}$) along a horizontal cross-section at the surface of the crust at time step 6: panels (a)–(g) correspond to model runs 1–7, respectively. Note that the contour values are not the same for all panels but, rather, were chosen to highlight the orientation of the *P*- and *Y*-shears in each run.

response to the imposed boundary conditions, regardless of the mechanical properties of the material.

Reducing Ar^P

To reduce Ar^P is equivalent to reducing the gravitational stresses with respect to the strength of the material. The main result is a small yet noticeable widening of the region of shear with respect to the depth of the modeled crustal layer as the main shear planes on either side of the shear zone tend to become less steep (Fig. 11c). This result is in good agreement with Bartlett *et al.*'s (1981) laboratory experiments on limestone. The distribution of deformation between the Riedel shears and the twin shear zones is quite similar to that of the first experiment (compare Fig. 10c with Fig. 10a). Dilatancy is more important in this third experiment (compare Fig. 9c with Fig. 9a). This is because lowering the gravitational stresses results in a reduction of the mean confining pressure; in other words, a larger proportion of the deforming body lies in the vicinity of the apex of the failure envelope where dilatancy is a maximum.

It must be stressed here that the reduction in Ar^P must be understood as a thinning of the modeled crustal block. Note, however, that reducing the thickness of the modeled layer by a factor of 2 only led to a small increase of the width-to-height ratio of the wedge-shaped zone of deformation. The width-to-height ratio of the zone of deformation is therefore approximately constant and quasi-independent of Ar^P. The proportionality between the depth of imposed wrenching and the width of the shear zone as postulated by Naylor *et al.* (1986) is thus confirmed, to first order, by the numerical model.

Pushing

In runs 4 and 5, the crustal block is, in addition to the imposed basal wrench, subjected to horizontal shortening in a direction normal to the strike of the shear zone. If the normal displacement is much smaller than the shear displacement (small $|r|$), the net result is a narrowing of the shear zone at its base (Fig. 11d) and a widening at its top. The overall shape of the shear zone (seen in cross-section) therefore resembles more that of a 'palm-tree' (or convex-upwards) structure (Horsfield 1977). This result is in good agreement with the observations of Horsfield (1977), Harding (1985), Naylor *et al.* (1986) and Richard & Cobbold (1989) both in the field and in scaled laboratory experiments.

For finite values of $|r|$ (run 5, Fig. 11e), the zone of crustal deformation becomes very wide and thrusting results in thickening of the crust. One must, however, realize that in the case of a finite $|r|$ value, the computed strain field is the superposition of two modes of deformation: strike-slip and thrusting. Strike-slip deformation is a maximum along the centre of the model (Fig. 11e) whereas thrusting takes place along two planes dipping at an angle of approximately $\pm \pi/4$ (Fig. 12). There is apparently little contamination of one mode of deformation by the other. In other words, two separate sets of structures develop: a series of near-vertical shear zones at the centre of the model and two outward-dipping thrust faults. The dip of the thrust planes ($\approx \pm\pi/4$) is in agreement with the 'theoretical' dip determined from simple stress distribution arguments (Braun 1993). Work is in progress to investigate the partitioning of deformation in 'general' transpressive

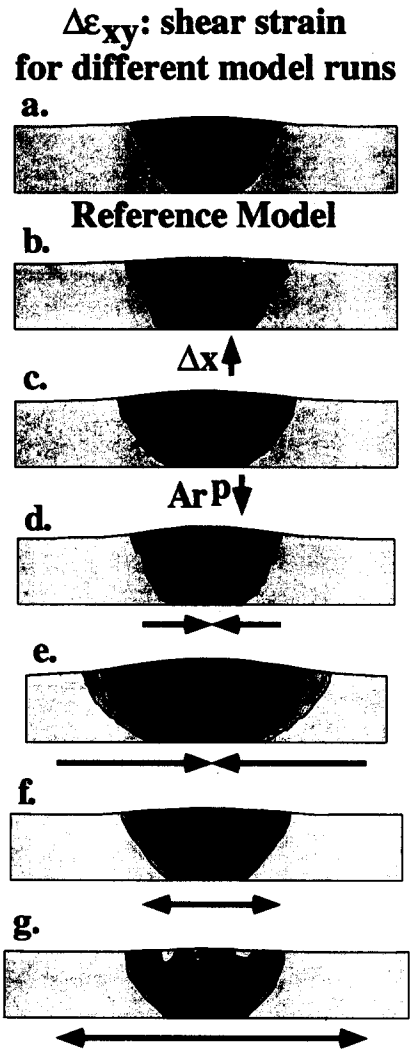

Fig. 11. Comparison between different model runs of the incremental horizontal strain ($\Delta\varepsilon_{xy}$) along a vertical cross-section halfway between the two side boundaries (at $y = 10L$) at time step 6: panels (a)–(g) correspond to model runs 1–7, respectively. The darkest areas are regions of maximum strain (> 11%); the lightest areas are regions of minimum strain (< 5%).

systems by exploring the complete range of r-values (from 0 to ∞).

For small values of $|r|$ (Fig. 10d), the P-shears form at a greater angle with respect to the direction of wrenching, a result similar to that of Naylor *et al.* (1986)

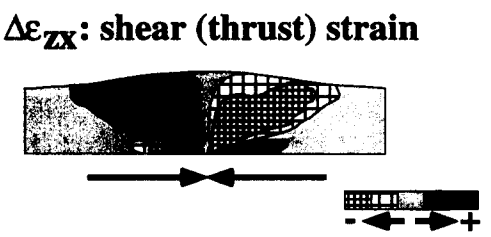

Fig. 12. Contours of the incremental vertical shear strain ($\Delta\varepsilon_{zx}$) along a vertical cross-section halfway between the two side boundaries (at $y = 10L$) at time step 6 for the model run 5 ($r = -0.3$). The shaded areas are regions of positive strain; the stippled areas are regions of negative strain.

Table 3. Values of γ at different time steps for runs 1, 5 and 7 as deduced from the computed principal stress orientations and magnitudes via equation (14)

Step	Run 1	Run 5	Run 7
2	12°	13°	12°
3	20°	16°	36°
4	22°	16°	38°
5	23°	17°	38°
6	21°	19°	40°

deduced from sand-box experiments. This relative 'rotation' of the P-shears is due to the rotation of the horizontal principal stresses. At high $|r|$ values (Fig. 10e), the distribution of shear at the surface is dominated by a narrow belt of intense shear deformation. There is some evidence of P-shears forming in this narrow region but they form a very low angle with the direction of wrenching (the y-axis). This apparently contradictory result is easily explained by recalling that the P-shear orientation is not only a function of the principal stress orientations but of their magnitude also (equation 12). Indeed, the surface orientation of the 'theoretical' Riedel shears calculated from the computed values of the principal stresses according to (12) are compared in Table 3 for runs 1 and 5 and show good agreement.

Dilatancy is strongly reduced (Fig. 9d) as the compressional component of the displacement results in increased confining pressure at all depths within the model.

Pulling

The results of runs 6 and 7 in which $r = 0.1$ and 0.3, respectively, are shown in Figs. 11(f) & (g) as contour plots of the shear strain increment in a vertical cross-section. In both cases, the imposed extensional displacement resulted in a concentration of the deformation along well-defined P-shears (Fig. 10e) and a definite concave-upwards or tulip-like shape for the deforming region seen in cross-section (Fig. 11f). The computations therefore agree very well with observations from the field and laboratory experiments (Naylor *et al.* 1986, Richard & Cobbold 1989): whereas palm-tree (or positive flower) structures develop in transpression experiments, tulip (or negative flower) structures develop in transtension.

At the surface, the strike of the P-shears measured from the direction of wrenching is smaller than in the pure strike-slip experiment (Fig. 10f) for small values of $|r|$, a result similar to the observations of Naylor *et al.* (1986); for large values of $|r|$, the P-shears are very well defined and form at a greater angle with respect to the y-direction (Fig. 10g) in qualitative accord with the simplified stress analysis (Table 3).

In the transtension experiment, dilatancy is large, even at intermediate crustal depths.

CONCLUSIONS

Murrell's failure criterion

The use of Murrell's extension in three dimensions of Griffith's failure criterion has led to interesting results regarding the geometry of faulting under strike-slip stress conditions.

(a) The spiral-like shape of Riedel shears as they extend below the surface to form so-called 'flower'-structures is a natural behaviour of faults in a material obeying Murrell's failure criterion. There is no need, as with the Coulomb–Navier criterion, to call upon a mechanical discontinuity in a deep basal layer along which the Riedel shears originate.

(b) Under special stress conditions, incipient fault geometry is, as in the case of the more classical Coulomb–Navier failure criterion, related to the orientation of the maximum and minimum principal stresses but also, and contrary to the Coulomb–Navier failure criterion, to the relative magnitude of the maximum and minimum principal stresses.

(c) The dilatant behaviour of rocks accompanying brittle shear deformation is approximately represented by combining an associative flow law with Murrell's failure criterion. Indeed, Murrell's theory predicts that dilatancy is inversely proportional to the square root of the confining pressure, a result in qualitative agreement with the results of laboratory experiments performed on rock samples characterized by low initial porosity.

Under specific stress conditions, however, relatively simple relationships have been derived (in this paper and by other authors) from Murrell's failure criterion that are of direct application to observational geology. More general identities could be derived by simple numerical computations. Ultimately, complex three-dimensional stress–strain analyses like the one presented in this paper are likely to flourish. All these factors should help in determining the applicability of Murrell's criterion to the brittle behaviour of crustal rocks. Deformation experiments at atmospheric pressure on analogue materials are unlikely to determine whether Murrell's criterion is applicable to crustal mechanics. Indeed, because the only material property in the expression of Murrell's criterion, the tensile strength, scales like a pressure (unlike the angle of internal friction, a dimensionless parameter), experiments to test the validity of Murrell's criterion must be done at high pressure (similar to those encountered in the Earth) or on material characterized by an extremely (possibly unrealistically) low tensile strength ($\approx$100 Pa).

Finite deformation numerical shear experiments

The three-dimensional finite element model has led to the following conclusions regarding the formation and evolution of strike-slip terranes.

(a) Oblique Riedel and *Y*-shears are the two dominant modes of shear deformation in a crust obeying Murrell's failure criterion.

(b) In the early stages of deformation, most of the deformation is taken up by strike-slip movement along a zone of diffuse shear aligned with the direction of imposed shear. This is a consequence of the finite elastic strength of the crust.

(c) After finite deformation, the shear zone widens and Riedel shears develop between two well-defined *Y*-shears.

(d) The orientation of the Riedel shears as a function of the direction and amplitude of the computed principal stresses is in semi-quantitative agreement with geometrical arguments derived from a simplified stress balance. Because their orientation is determined by the stress distribution after finite deformation, the Riedel shears are equivalent to the *P*-shears defined by Naylor *et al.* (1986).

(e) The model predicts the formation of spiral-like Riedel shears similar to the flower structures observed in the field and in the laboratory.

(f) As the region of imposed wrenching at the base of the modelled crust is widened, the shear zone widens and Riedel shears take up most of the deformation at the expense of the bounding *Y*-shears.

(g) The width of the shear zone is proportional to the thickness of the sheared layer, but the relationship is not linear.

(h) The superposition of a normal component of deformation to the imposed basal wrenching movement leads to profound changes in the morphology of the shear zone: transpression results in a widening of the shear zone and the formation of 'palm-tree' structures whereas transtension leads to a narrowing of the shear zone and the formation of 'tulip' structures, in accordance with observations and laboratory experiments.

(i) The orientation of the Riedel shears is also affected by the presence of an in-plane stress: a small amount of compression rotates the *P*-shears away from the direction of wrenching whereas a large amount of compression rotates them towards the direction of wrenching; a small amount of tension rotates the Riedels towards the direction of wrenching whereas a large amount of tension rotates them away from the direction of wrenching.

Acknowledgements—The author wishes to thank two anonymous reviewers for very constructive comments made on an earlier version of this manuscript. Some of the calculations upon which this work is based were carried out using the Fujitsu VP-2200 of the Australian National University Supercomputer Facility.

REFERENCES

Bartlett, W. L., Friedman, M. & Logan, J. M. 1981. Experimental folding and faulting of rocks under confining pressure. Part IX. Wrench faults in limestone layers. *Tectonophysics* **79**, 255–277.

Bassi, G. 1991. Factors controlling the style of continental rifting: insights from numerical modelling. *Earth Planet. Sci. Lett.* **105**, 430–452.

Braun, J. 1993. Three-dimensional numerical modeling of compressional orogenies: thrust geometry and oblique convergence. *Geology* **21**, 153–156.

Braun, J. & Beaumont, C. 1987. Styles of continental rifting: results from dynamic models of lithospheric extension. In: *Sedimentary*

Basins and Basin-forming Mechanisms (edited by Beaumont, C. & Tankard, A. J.). *CSPG Mem.* **12**, 241–258.
Burford, R. O., Castle, R. O., Church, J. P., Kinoshita, W. T., Kirby, S. H., Ruthven, R. T. & Savage, J. C. 1972. Preliminary measurements of tectonic movements. In: *The San Fernando, California, Earthquake of February* 9, 1971. *Prof. Pap. U.S. geol. Surv.* **733**, 80–85.
Chéry, J., Vilotte, J.-P. & Daignières, M. 1991. Thermo-mechanical evolution of a thinned continental lithosphere under compression: implications for the Pyrennees. *J. geophys. Res.* **96**, 4385–4412.
Coulomb, C. A. 1773. Sur une application des règles de Maximis and Minimis à quelques problèmes de statique relatifs à l'Architecture. Académie Royale des Sciences. *Mém. math. & phys. divers savants* **7**, 343–383.
Edmond, J. M. & Paterson, M. S. 1972. Volume changes during the deformation of rocks at high pressures. *Int. J. Rock Mech. & Mining Sci.* **9**, 161–182.
Fung, Y. C. 1965. *Foundations of Solid Mechanics*. Prentice-Hall, New Jersey.
Griffith, A. A. 1921. The phenomena of rupture and flow in solids. *Phil. Trans. R. Soc. Lond.* **A221**, 163–198.
Harding, T. P. 1985. Seismic characteristics and identification of negative flower structures, positive flower structures, and positive structural inversion. *Bull. Am. Ass. petrol. Geol.* **69**, 582–600.
Horsfield, W. T. 1977. An experimental approach to basement controlled faulting. In: *Fault Tectonics in NW Europe* (edited by Frost, R. T. C. & Dikkers, A. J.). *Geologie Mijnb.* **56**, 363–370.
Hughes, T. J. R. & Winget, J. 1980. Finite rotation effects in numerical integration of rate constitutive equations arising in large-deformation analysis. *Int. J. Num. Meth. Engng.* **15**, 1862–1867.
Mandl, G. 1988. Mechanics of tectonic faulting: models and basic concepts. In: *Developments in Structural Geology, Volume* 1 (edited by Zwart, H. J.). Elsevier, Amsterdam.
McMahon Moore, J. 1979. Tectonics of the Najd transcurrent fault system, Saudi Arabia. *J. geol. soc. Lond.* **136**, 441–454.
Murrell, S. A. F. 1958. The strength of coal under triaxial compression. In: *Mechanical Properties of Non-metallic Brittle Materials* (edited by Walton, W. H.). Butterworth, London, 123–146.
Murrell, S. A. F. 1963. A criterion for brittle fracture of rocks and concrete under triaxial stress and the effect of pore pressure on the criterion. Proceedings of the Fifth Rock Mechanics Symposium, University of Minnesota. In: *Rock Mechanics* (edited by Fairhurst, C.). Pergamon Press, Oxford, 563–577.
Murrell, S. A. F. 1965. The effect of triaxial stress systems on the strength of rocks at atmospheric temperatures. *Geophys. J. R. astr. Soc.* **10**, 231–281.
Naylor, M. A., Mandl, G. & Sijpestein, C. H. K. 1986. Fault geometries in basement induced wrench faulting under different initial stress states. *J. Struct. Geol.* **7**, 737–752.
Nur, A., Ron, H. & Scotti, O. 1986. Fault mechanics and the kinematics of block rotation. *Geology* **14**, 746–749.
Nur, A., Ron, H. & Scotti, O. 1989. Kinematics and mechanics of tectonic block rotations. In: *Slow Deformation and Transmission of Stress in the Earth* (edited by Cohen, S. V. and Vanicek, P.). *Am. Geophys. Un. Geophys. Monogr.* **49**, 31–46.
Owen, D. R. J. & Hinton, E. 1980. *Finite Elements in Plasticity: Theory and Practice*. Pineridge Press, Swansea, U.K.
Paterson, M. S. 1978. *Experimental Rock Deformation: The Brittle Field*. Springer, Berlin.
Raleigh, C. B. & Burford, R. O. 1969. Tectonics of the San Andreas fault system. Strain studies. *Eos* **50**, 380–381.
Richard, P. & Cobbold, P. 1989. Structures en fleurs positives et décrochements crustaux: modélisation analogique et interprétation mécanique. *C. r. hebd. Séanc. Acad. Sci., Paris, Sér II* **308**, 553–560.
Riedel, W. 1929. Zur Mechanik geologischer Brucherscheinungen. *Centralbl. Miner. Abt. B* **1929**, 354–368.
Scholz, C. H. 1968. Microfracturing and the inelastic deformation of rocks in compression. *J. geophys. Res.* **73**, 1417–1432.
Wilcox, R. E., Harding, T. P. & Seely, D. R. 1973. Basic wrench tectonics. *Bull. Am. Ass. Petrol. Geol.* **57**, 74–96.
Wilkins, M. L. 1963. Calculation of elastic-plastic flow. In: *Methods of Computational Physics, Volume* 3 (edited by Alder, B. *et al.*). Academic Press, New York.
Woodcock, N. H. & Fischer, M. 1986. Strike-slip duplexes. *J. Struct. Geol.* **8**, 725–735.
Zhang, S. 1992. Fluid transport properties of calcite rocks. Unpublished Ph.D. thesis, Australian National University, Canberra, Australia.
Zienkiewicz, O. C. 1977. *The Finite Element Method* (3rd edn). McGraw-Hill, London.

APPENDIX 1

In the space of principal stresses (σ_1, σ_2, σ_3), Murrell's yield envelope (equation 8a) may be expressed as follows:

$$F = (\sigma_1 - \sigma_2)^2 + (\sigma_2 - \sigma_3)^2 + (\sigma_3 - \sigma_1)^2 + 24T_0(\sigma_1 + \sigma_2 + \sigma_3) = 0 \tag{A1}$$

or, in matrix form:

$$F = X^{\mathrm{T}}HX + 2B^{\mathrm{T}}X = 0, \tag{A2}$$

where

$$X = (\sigma_1\ \sigma_2\ \sigma_3) \tag{A3}$$

$$H = \begin{pmatrix} \frac{1}{3} & -\frac{1}{6} & -\frac{1}{6} \\ -\frac{1}{6} & \frac{1}{3} & -\frac{1}{6} \\ -\frac{1}{6} & -\frac{1}{6} & \frac{1}{3} \end{pmatrix} \tag{A4}$$

and

$$B = 2T_0 \begin{pmatrix} 1 \\ 1 \\ 1 \end{pmatrix}. \tag{A5}$$

The direction of the normal, N, to the yield surface at a point X on the surface may be obtained by differentiating F with respect to the principal stress components:

$$N = HX + B. \tag{A6}$$

The normal projection from a point X_0 outside of the yield envelope is given by:

$$X_{\mathrm{P}} = X_0 + \alpha(HX_{\mathrm{P}} + B) \tag{A7}$$

or

$$X_{\mathrm{P}} = (I - \alpha H)^{-1}(X_0 + \alpha B), \tag{A8}$$

where I is the identity matrix. The value of α may be obtained from the following expression, derived from the assumption that the projection, X_{p}, lies on the yield surface ($F(X_{\mathrm{p}}) = 0$):

$$\frac{X_0^{\mathrm{T}}HX_0}{\left(1 - \frac{\alpha}{2}\right)^2} + 2\mathrm{B}^{\mathrm{T}}X_0 + 24\alpha T_0^2 = 0 \tag{A9}$$

It is interesting to notice that α is the solution of a third-order equation which possesses one or three solutions. One may show that the stress space may be divided into two separate regions where there exist either one or three normal projections onto the yield envelope. In the finite element calculations, we choose the projection closest to the elastic stress state.

APPENDIX 2

The mid-point strain, $\varepsilon_{ij}^{1/2}$, is defined as follows:

$$\varepsilon_{ij}^{1/2} = \frac{1}{2}\left(\frac{\partial u_i}{\partial x_j^{1/2}} + \frac{\partial u_j}{\partial x_i^{1/2}}\right), \tag{A10}$$

where the u_i are the components of the incremental displacement vector and the $x_i^{1/2}$ are the spatial co-ordinates of the deformed material in a configuration half-way between the pre- and post-deformation configurations, x^0 and x^1:

$$x_i^{1/2} = x_i^0 + \frac{(x_i^1 - x_i^0)}{2}. \tag{A11}$$

One may show (Hughes & Winget 1980) that the mid-point strain is a second-order approximation to the true measure of strain in large deformation analyses and therefore carries the same kinematic information as the incremental Eulerian strain or incremental Lagrangian strain. The main advantages of the mid-point strain over other large deformation measures result from its similitude to the infinitesimal linear strain: (a) a simple, linear expression in terms of displacement

derivatives and (b) its trace is a second-order approximation to volume change.

During finite deformation that may involve finite rotations, the stress rate $\dot{\sigma}$ (or rate of change of the Cauchy stress over the deformation interval), is not properly transformed. The stress rate is not an objective quantity (Hughes & Winget 1980). The Green–Naghdi stress rate defined as:

$$\sigma^* = \dot{\sigma} + \sigma \times w - w \times \sigma, \tag{A12}$$

where

$$w = \dot{R}R^{-1} \tag{A13}$$

and R is the rotation matrix (a proper-orthogonal matrix formed from the anti-symmetric part of the deformation gradient), is an objective quantity and possesses an interesting property:

$$\dot{\sigma}_R = R^T \sigma^* R, \tag{A14}$$

where

$$\sigma_R = R^T \sigma R. \tag{A15}$$

It follows that a rather complex, but correct, measure of stress change (A12) is transformed in a rather simple expression (A14) following an arbitrary change of coordinates.

The complete finite deformation algorithm may be summarized as follows:

(a) compute the incremental mid-point strains, $\varepsilon^{1/2}$;

(b) compute the rotation matrices, R^0, $R^{1/2}$ and R^1 corresponding to the total deformation in configurations 0, ½ and 1, respectively;

(c) transform the initial stress and mid-point strain tensors according to $\sigma_R^0 = (R^0)^T \sigma^0 R^0$ and, $\varepsilon_R^{1/2} = (R^{1/2})^T \varepsilon^{1/2} R^{1/2}$;

(d) calculate the new 'rotated' stresses, σ_R^1, from the previous 'rotated' stresses, σ_R^0, and the 'rotated' mid-point strain, $\varepsilon_R^{1/2}$, following the elasto-plastic constitutive relationship via the radial-return algorithm;

(e) transform back the 'rotated' stresses according to $\sigma^1 = R\sigma^1{}_R R^T$.

The only remaining step is to design an efficient way of deriving the rotation matrix R by performing the polar decomposition:

$$F = RU, \tag{A16}$$

of the deformation gradient, F, into its symmetric, U, and anti-symmetric, R parts. This may be easily done by calculating the right Cauchy strain tensor:

$$C = F^T F = U^T U, \tag{A17}$$

and computing its square root by making use of the Cayley–Hamilton theorem:

$$U = \frac{D - (I_1^2 - I_2)C - I_1 I_3 I}{I_3 - I_1 I_2}, \tag{A18}$$

where

$$D = C^T C, \tag{A19}$$

I is the identity matrix and I_1, I_2 and I_3 are the invariants of U obtained from the invariants of C (I_1^C, I_2^C and I_3^C via:

$$\begin{aligned} I_3 &= \sqrt{I_3^C} \\ I_2 &= \sqrt{I_1^C + 2I_3 I_1} \\ I_1 &= \sqrt{I_2^C + 2I_2}. \end{aligned} \tag{A20}$$

Once U has been found, R may be obtained from:

$$R = FU^{-1}. \tag{A21}$$

APPENDIX 3

The incremental mechanical work following an incremental plastic deformation, $d\varepsilon^p$, at stress level σ is given by:

$$d\Omega = d\varepsilon^p \dot{\sigma}, \tag{A22}$$

which, according to the associative flow law, may also be expressed as:

$$d\Omega = -\lambda 12 T_0 p, \tag{A23}$$

or, in terms of the second invariant of the plastic strain increment tensor:

$$d\Omega = \sqrt{-12 T_0 p E_{2D}^p}. \tag{A24}$$

The combination of Murrell's criterion and an associative flow law therefore predicts that the incremental plastic work is proportional to the deviatoric strain increment and the square root of the pressure.